

Frequency-dependent Alfvén-wave propagation in the solar wind:
Onset and suppression of parametric decay instability

MUNEHITO SHODA,¹ TAKAAKI YOKOYAMA,¹ AND TAKERU K. SUZUKI²

¹*Department of Earth and Planetary Science, The University of Tokyo, Hongo, Bunkyo-ku, Tokyo, 113-0033, Japan*

²*School of Arts & Sciences, The University of Tokyo, 3-8-1, Komaba, Meguro, Tokyo, 153-8902, Japan*

ABSTRACT

Using numerical simulations we investigate the onset and suppression of parametric decay instability (PDI) in the solar wind, focusing on the suppression effect by the wind acceleration and expansion. Wave propagation and dissipation from the coronal base to 1 au is solved numerically in a self-consistent manner; we take into account the feedback of wave energy and pressure in the background. Monochromatic waves with various injection frequencies f_0 are injected to discuss the suppression of PDI, while broadband waves are applied to compare the numerical results with observation. We find that high-frequency ($f_0 \gtrsim 10^{-3}$ Hz) Alfvén waves are subject to PDI. Meanwhile, the maximum growth rate of the PDI of low-frequency ($f_0 \lesssim 10^{-4}$ Hz) Alfvén waves becomes negative due to acceleration and expansion effects. Medium-frequency ($f_0 \approx 10^{-3.5}$ Hz) Alfvén waves have a positive growth rate but do not show the signature of PDI up to 1 au because the growth rate is too small. The medium-frequency waves experience neither PDI nor reflection so they propagate through the solar wind most efficiently. The solar wind is shown to possess frequency-filtering mechanism with respect to Alfvén waves. The simulations with broadband waves indicate that the observed trend of the density fluctuation is well explained by the evolution of PDI while the observed cross-helicity evolution is in agreement with low-frequency wave propagation.

Keywords: magnetohydrodynamic(MHD) — methods:numerical — solar wind — Sun:corona

1. INTRODUCTION

It is widely accepted that Alfvén waves (Alfvén 1942) play an important role in the heating (Alfvén 1947; Osterbrock 1961; Matthaeus et al. 1999) and acceleration (Belcher 1971; Jacques 1977; Heinemann & Olbert 1980) of the solar wind. Indeed, Alfvén waves are observed in the solar atmosphere (De Pontieu et al. 2007; Tomczyk et al. 2007; McIntosh et al. 2011; Srivastava et al. 2017) and solar wind (Coleman 1968; Belcher & Davis 1971). Nonthermal line width (Banerjee et al. 2009; Hahn & Savin 2013) and Faraday-rotation fluctuations (Hollweg et al. 1982, 2010) also indicate the existence of Alfvén waves in the corona. Meanwhile, the dissipation process of Alfvén waves in the corona and solar wind is still under discussion. Since the amount and location of Alfvén-wave dissipation vary with respect to the mechanism and strongly affect the coronal temperature and

wind velocity (Hansteen & Velli 2012), clarifying the elemental processes is important not only for plasma physics but also for space weather.

There are several processes of Alfvén-wave dissipation. If there are counter-propagating Alfvén waves, Alfvén-wave turbulence (Iroshnikov 1964; Kraichnan 1965; Dobrowolny et al. 1980; Goldreich & Sridhar 1995) evolves. In the corona and solar wind, because of the inhomogeneity, Alfvén waves partially reflect (Ferraro & Plumpton 1958; Heinemann & Olbert 1980; An et al. 1990; Velli 1993; Cranmer & van Ballegoijen 2005) and Alfvén-wave turbulence is sustained (Dmitruk & Matthaeus 2003; Oughton et al. 2006). This reflection-driven Alfvén-wave turbulence is frequently studied (Matthaeus et al. 1999; Dmitruk et al. 2002; Verdini & Velli 2007; Perez & Chandran 2013; van Ballegoijen & Asgari-Targhi 2016), and some models explain the heating and acceleration of the solar wind self-consistently (Cranmer et al. 2007; Verdini et al. 2010). Alfvén-wave turbulence is also important for the energy cascade and the formation of the power spectrum (Verdini et al. 2012; van Ballegoijen & Asgari-Targhi 2017).

When the Alfvén velocity is inhomogeneous perpendicular to the magnetic field lines, phase mixing begins (Heyvaerts & Priest 1983; De Groof & Goossens 2002; Goossens et al. 2012). The density variation across the magnetic field lines is observed in the corona (Tian et al. 2011; Raymond et al. 2014), and this indicates the possibility of phase mixing. Several studies show the role of phase mixing and related phenomena in the solar atmosphere (Antolin et al. 2015; Kaneko et al. 2015). Recently, it was numerically shown that phase mixing can generate turbulent structure (Magyar et al. 2017).

Since the amplitude of an Alfvén wave is not small and the plasma beta is low (Gary 2001; Iwai et al. 2014; Bourdin 2017), the (extended) corona and solar wind are preferable locations for the development of parametric decay instability (PDI). PDI is a type of instability of an Alfvén wave (Galeev & Oraevskii 1963; Sagdeev & Galeev 1969; Goldstein 1978; Derby 1978) and was recently observed in laboratory plasma (Dorfman & Carter 2016) and in the solar wind (Bowen et al. 2018). As a result of PDI, a large-amplitude longitudinal wave is generated (Hoshino & Goldstein 1989; Del Zanna et al. 2001), and the plasma is heated up by the resultant shock wave. Suzuki & Inutsuka (2005, 2006) demonstrated that, without Alfvén-wave turbulence, the coronal heating and solar-wind acceleration are explained self-consistently by PDI. These studies were extended to two dimensions (2D) by Matsumoto & Suzuki (2012, 2014). In addition, the cross-helicity evolution in the fast solar wind (Bavassano et al. 1982, 2000) might be due to PDI (Malara & Velli 1996; Malara et al. 2000; Shoda & Yokoyama 2016). Chandran (2018) also argued that the $1/f$ spectrum observed in the fast solar wind (Bruno & Carbone 2013) possibly results from PDI.

We note that Alfvén-wave turbulence and PDI are not independent of each other, because PDI generates large-amplitude backscattered Alfvén waves (Sagdeev & Galeev 1969; Goldstein 1978) and enhances the heating by Alfvén-wave turbulence. Shoda et al. (2018) showed that, due to PDI, the turbulence heating rate per unit mass increases ($\sim 10^{11}$ erg g^{-1} s^{-1}) compared with the reduced- magnetohydrodynamic MHD (without-PDI) value ($\sim 10^{10}$ erg g^{-1} s^{-1}) (Perez & Chandran 2013; van Ballegoijen & Asgari-Targhi 2016).

Amongst the aforementioned dissipation processes, we focus on PDI in this study. The PDI of monochromatic Alfvén waves in a time-independent, uniform background with MHD approximation is well studied. In the limit of $\beta \ll 1$ and $\eta = \delta B/B_0 \ll 1$ where B_0 and δB denote the mean and fluctuating magnetic field, respectively, the growth rate is given as (Galeev &

Oraevskii 1963; Sagdeev & Galeev 1969)

$$\gamma/\omega_0 = \frac{1}{2}\eta\beta^{-1/4}, \quad (1)$$

where ω_0 is the angular frequency of the parent wave. Here we define β as

$$\beta = c_s^2/v_A^2, \quad (2)$$

where c_s and v_A denote the sound and Alfvén speed, respectively. The general dispersion relation that considers full four-wave interaction (Lashmore-Davies 1976) is given by Goldstein (1978) and Derby (1978) as

$$\begin{aligned} (\omega - k)(\omega^2 - \beta k^2) \left[(\omega + k)^2 - 4 \right] \\ = \eta^2 k^2 (\omega^3 + k\omega^2 - 3\omega + k), \end{aligned} \quad (3)$$

where ω and k are normalized by the parent-wave frequency ω_0 and wavenumber k_0 . In this study, we call Eq. (3) the Goldstein–Derby dispersion relation. By solving Eq. (3), Goldstein (1978) confirmed that the classical understanding that the parent wave decays into a forward acoustic wave and a backward Alfvén wave is correct in the low-beta regime. In the high-beta plasma, however, the behavior of the instability changes (Jayanti & Hollweg 1993). The linear stage of this *ideal* (monochromatic, time-independent, and uniform) case is well understood. The nonlinear stage of PDI is also frequently studied using numerical simulation. Hoshino & Goldstein (1989) studied the linear-to-nonlinear evolution of PDI. This study was extended to multi-dimensional simulations in both low- and high-beta cases (Ghosh & Goldstein 1994; Ghosh et al. 1994). Del Zanna et al. (2001) investigated the evolution of PDI with different plasma parameters, different dimensions and different boundary conditions to show the robustness of PDI. Recently, the three-dimensional (3D) hybrid simulation of PDI-driven turbulence has been studied (Fu et al. 2017).

There are several studies on the linear growth rate of PDI under *non-ideal* situations. Two-fluid and kinetic simulations were performed (Terasawa et al. 1986; Nariyuki et al. 2008). The PDI of non-monochromatic Alfvén waves tends to have a smaller growth rate (Cohen & Dewar 1974; Umeki & Terasawa 1992; Malara & Velli 1996; Malara et al. 2000). If the background is turbulent, the growth rate is quenched compared with the *ideal* value (Shi et al. 2017). The solar wind acceleration and expansion also work to reduce the growth rate (Tenerani & Velli 2013; Del Zanna et al. 2015). Recently the effect of temperature anisotropy on PDI has also been also studied (Tenerani et al. 2017).

Specifically in the solar wind close to the Sun, wind acceleration and expansion play an important role. Such effects are frequently studied using a local co-moving box in the so-called accelerating expanding box (AEB) model (Velli et al. 1992; Grappin et al. 1993; Grappin & Velli 1996; Tenerani & Velli 2017). One problem with the AEB model is that the dynamics and energetics are not self-consistent; initially, we have to assume the background quantities such as flow speed or Alfvén speed and ignore the feedback of wave heating and acceleration on them. Our motivation is to test the idea obtained from the AEB model using a non-local simulation box that extends from the corona to the distant heliosphere.

This paper is organized as follows. In Section 2, we describe the basic equations, numerical scheme, and boundary conditions used in this study. Section 3 and Section 4 describe the results with monochromatic wave injection and broadband wave injection, respectively. We summarize this paper in Section 5

2. NUMERICAL METHOD

2.1. Basic equations and setting

We used the same equations as those in Shoda et al. (2018) and considered a one-dimensional system whose coordinate r is curved along the background magnetic field line. The basic equations used were

$$\frac{\partial}{\partial t} (\rho r^2 f) + \frac{\partial}{\partial r} (\rho v_r r^2 f) = 0, \quad (4)$$

$$\begin{aligned} \frac{\partial}{\partial t} (\rho v_r r^2 f) + \frac{\partial}{\partial r} \left[\left(\rho v_r^2 + p + \frac{\mathbf{B}_\perp^2}{8\pi} \right) r^2 f \right] \\ = \left(p + \frac{\rho \mathbf{v}_\perp^2}{2} \right) \frac{d}{dr} (r^2 f) - \rho g r^2 f, \end{aligned} \quad (5)$$

$$\begin{aligned} \frac{\partial}{\partial t} (\rho \mathbf{v}_\perp r^3 f^{3/2}) + \frac{\partial}{\partial r} \left[\left(\rho v_r \mathbf{v}_\perp - \frac{B_r \mathbf{B}_\perp}{4\pi} \right) r^3 f^{3/2} \right] \\ = -\hat{\boldsymbol{\eta}}_1 \cdot \rho \mathbf{v}_\perp r^3 f^{3/2} - \hat{\boldsymbol{\eta}}_2 \cdot \sqrt{\frac{\rho}{4\pi}} \mathbf{B}_\perp r^3 f^{3/2}, \end{aligned} \quad (6)$$

$$\begin{aligned} \frac{\partial}{\partial t} (\mathbf{B}_\perp r \sqrt{f}) + \frac{\partial}{\partial r} \left[(\mathbf{B}_\perp v_r - B_r \mathbf{v}_\perp) r \sqrt{f} \right] \\ = -\hat{\boldsymbol{\eta}}_1 \cdot \mathbf{B}_\perp r \sqrt{f} - \hat{\boldsymbol{\eta}}_2 \cdot \sqrt{4\pi} \rho \mathbf{v}_\perp r \sqrt{f}, \end{aligned} \quad (7)$$

$$\frac{d}{dr} (B_r r^2 f) = 0, \quad (8)$$

$$\begin{aligned} \frac{\partial}{\partial t} \left[\left(e + \frac{1}{2} \rho v^2 + \frac{\mathbf{B}^2}{8\pi} \right) r^2 f \right] \\ + \frac{\partial}{\partial r} \left[\left(e + p + \frac{1}{2} \rho v^2 + \frac{\mathbf{B}_\perp^2}{4\pi} \right) v_r r^2 f - B_r \frac{\mathbf{B}_\perp \cdot \mathbf{v}_\perp}{4\pi} r^2 f \right] \\ = r^2 f (-\rho g v_r + Q_{\text{cond}}), \end{aligned} \quad (9)$$

$$e = \frac{p}{\Gamma - 1}, \quad p = \frac{\rho k_B T}{\mu}. \quad (10)$$

See Appendix in Shoda & Yokoyama (2018) for the derivation. We denoted the perpendicular components of \mathbf{X} as $\mathbf{X}_\perp = X_x \mathbf{e}_x + X_y \mathbf{e}_y$, and we assumed that the plasma is composed of only hydrogen and is fully ionized in the entire simulation region. Therefore, the mean molecular mass μ satisfied $\mu = 0.5m_p$ where m_p is the proton mass. Γ is the adiabatic specific heat: $\Gamma = 5/3$.

f is the expansion factor of the flux tube (Levine et al. 1977; Wang & Sheeley 1990; Arge & Pizzo 2000). In this study, following Kopp & Holzer (1976) and Verdini et al. (2010), we assumed

$$f(r) = \frac{f_{\text{exp}} \exp[(r - r_f)/\sigma] + f_1}{\exp[(r - r_f)/\sigma] + f_1}, \quad (11)$$

where $f_1 = 1 - f_{\text{exp}} \exp[(R_\odot - r_f)/\sigma]$, $f_{\text{exp}} = 10$, $r_f = 1.3R_\odot$ and $\sigma = 0.5R_\odot$.

$\hat{\boldsymbol{\eta}}_1$ and $\hat{\boldsymbol{\eta}}_2$ are coefficient tensors that represent phenomenological turbulent decay.

$$\hat{\boldsymbol{\eta}}_1 = \frac{c_d}{4\lambda} \begin{pmatrix} |z_x^+| + |z_x^-| & 0 \\ 0 & |z_y^+| + |z_y^-| \end{pmatrix}, \quad (12)$$

$$\hat{\boldsymbol{\eta}}_2 = \frac{c_d}{4\lambda} \begin{pmatrix} |z_x^+| - |z_x^-| & 0 \\ 0 & |z_y^+| - |z_y^-| \end{pmatrix}, \quad (13)$$

where $z_{x,y}^\pm$ are Elsässer variables (Elsässer 1950):

$$z_{x,y}^\pm = v_{x,y} \mp B_{x,y}/\sqrt{4\pi\rho}. \quad (14)$$

Shoda et al. (2018) showed that these terms are a natural extension of a widely used phenomenological model of Alfvén-wave turbulence (Hossain et al. 1995; Dmitruk et al. 2002; Verdini & Velli 2007; Chandran & Hollweg 2009). $c_d = 0.1$ was chosen in this study (van Ballegooijen & Asgari-Targhi 2017). λ is the perpendicular correlation length of turbulence. We assumed that the correlation length is proportional to the flux-tube radius:

$$\lambda \propto B_r^{-1/2}. \quad (15)$$

Using the phenomenological turbulence term together with Eq. (15), both local (Cranmer et al. 2007; Verdini et al. 2010; Lionello et al. 2014; Shoda et al. 2018) and global (van der Holst et al. 2014) simulations succeeded in modeling the corona and solar wind. The correlation length at the coronal base (λ_0) is

$$\lambda_0 = 1 \text{ Mm}. \quad (16)$$

This is based on the assumption that Alfvén waves are generated inside the magnetic patches on the photosphere and propagate upward along the flux tube (van Ballegooijen et al. 2011).

Q_{cond} is the heating by thermal conduction given as

$$Q_{\text{cond}} = -\nabla \cdot \mathbf{q}_{\text{cond}} = -\frac{1}{r^2 f} \frac{\partial}{\partial r} (r^2 f q_{\text{cond}}), \quad (17)$$

where \mathbf{q}_{cond} is the conductive flux and q_{cond} represents its radial component. The conductive flux is a combination of Spitzer-Härm flux (Spitzer & Härm 1953) and free-streaming flux (Hollweg 1974, 1976) given as

$$q_{\text{cond}} = \xi q_{\text{SH}} + (1 - \xi) q_{\text{FS}}, \quad \xi = \max\left(1, \frac{\rho}{\rho_{\text{SW}}}\right) \quad (18)$$

where $\rho_{\text{SW}} = 10^{-21} \text{ g cm}^{-3}$ and

$$q_{\text{SH}} = -\kappa_0 T^{5/2} \frac{\partial}{\partial r} T, \quad (19)$$

$$q_{\text{FS}} = \frac{3}{4} \alpha p v_r. \quad (20)$$

In GGS-Gaussian units, $\kappa_0 \approx 10^{-6}$. We fixed $\alpha = 2$ in this study.

Radiative cooling is ignored because of its small contribution to the coronal energy budget (Matsumoto & Suzuki 2014; van Ballegooijen & Asgari-Targhi 2016). The coronal base is cooled down by keeping the bottom temperature fixed.

2.2. Numerical scheme and boundary conditions

We solved the basic equations (4)-(10) from the coronal base ($r = 1.014 R_{\odot}$) to 1 au ($r = 215 R_{\odot}$). Furthermore, we applied 50 000 uniform grid points to resolve the computational domain. The Harten-Lax-van Leer-discontinuities (HLLD) approximated Riemann solver (Miyoshi & Kusano 2005) with 2nd-order monotone upstream-centered schemes for conservation law (MUSCL) reconstruction (van Leer 1979) was used to calculate the numerical flux, while the 3rd-order strong stability preserving (SSP) Runge-Kutta method (Shu & Osher 1988) was used for time integration.

The free boundary condition was imposed on the boundary at 1 au. We confirmed that the boundary condition at 1 au does not affect the calculation because the super-sonic and super-Alfvénic solar wind is formed in a quasi-steady state. This is why we did not need to apply the transmitting boundary condition (Thompson 1987; Del Zanna et al. 2001; Suzuki & Inutsuka 2006). As for the lower boundary, the conditions were as follows. Here we denoted the lower-boundary values with subscript 0. The mass density ρ , temperature T , and radial magnetic field strength B_r were fixed to

$$\rho_0 = 8.5 \times 10^{-16} \text{ g cm}^{-3}, \quad T_0 = 4 \times 10^5 \text{ K}, \quad B_{r,0} = 10 \text{ G}. \quad (21)$$

The quantity $B_{r,0}/f_{\text{exp}}$ controls the solar-wind velocity (Suzuki 2004, 2006; Fujiki et al. 2015; Réville & Brun 2017). According to Fujiki et al. (2015), our setting of ($B_{r,0}/f_{\text{exp}} = 1 \text{ G}$) approximately corresponds to 650 km s^{-1} in terms of asymptotic solar wind velocity.

We applied the free boundary conditions for the radial velocity and inward Elsässer variable:

$$\left. \frac{\partial}{\partial r} v_r \right|_0 = 0, \quad \left. \frac{\partial}{\partial r} z^- \right|_0 = 0, \quad (22)$$

where $z^- = \mathbf{v}_{\perp} + \mathbf{B}_{\perp}/\sqrt{4\pi\rho}$. As for the upward Elsässer variable, $z^+ = \mathbf{v}_{\perp} - \mathbf{B}_{\perp}/\sqrt{4\pi\rho}$, we applied monochromatic (Section 3) or broadband (Section 4) wave injections. In both cases, the root-mean-square value of the transverse velocity $v_{\text{rms},0}$ was fixed to $v_{\text{rms},0} = 32 \text{ km s}^{-1}$. In terms of the upward Elsässer variable, the root-mean-square value was $z_{\text{rms},0}^+ = 2v_{\text{rms},0}$, because $|z_{x,y}^+| \gg |z_{x,y}^-|$ at the coronal base and

$$\begin{aligned} z_{\text{rms},0}^+ &= \sqrt{z_x^{+2} + z_y^{+2}} \\ &\simeq \sqrt{(z_x^+ + z_x^-)^2 + (z_y^+ + z_y^-)^2} \\ &= \sqrt{4(v_x^2 + v_y^2)} = 2v_{\text{rms},0}. \end{aligned} \quad (23)$$

Note that the injected energy flux F_0 was kept constant:

$$F_0 = \frac{1}{4} \rho z_0^{+2} v_{A,0} = 8.4 \times 10^5 \text{ erg cm}^{-3} \text{ s}^{-1}. \quad (24)$$

This was larger than the required amount of energy injection required to sustain the solar wind in the open field regions (Withbroe & Noyes 1977).

3. MONOCHROMATIC-WAVE INJECTION

We first applied the monochromatic wave injections with different frequencies to discuss the basic properties. The boundary condition of the upward Elsässer variable was

$$z_{x,0}^+ = 2v_{\text{rms},0} \sin(2\pi f_0 t), \quad (25)$$

$$z_{y,0}^+ = 2v_{\text{rms},0} \cos(2\pi f_0 t), \quad (26)$$

where f_0 is the injection frequency.

3.1. Quasi-steady state

Figure 1 shows the snapshots of the quasi-steady states of different injection frequencies: $f_0 = 10^{-2.5} \text{ Hz}$ (blue), $10^{-3.5} \text{ Hz}$ (green), $10^{-4.5} \text{ Hz}$ (red). Panels indicate from top to bottom the mass density ρ , temperature T , radial velocity v_r , and Elsässer variables $z^{\pm} = \sqrt{z_x^{\pm 2} + z_y^{\pm 2}}$ (transparent: z^+ , dashed: z^-).

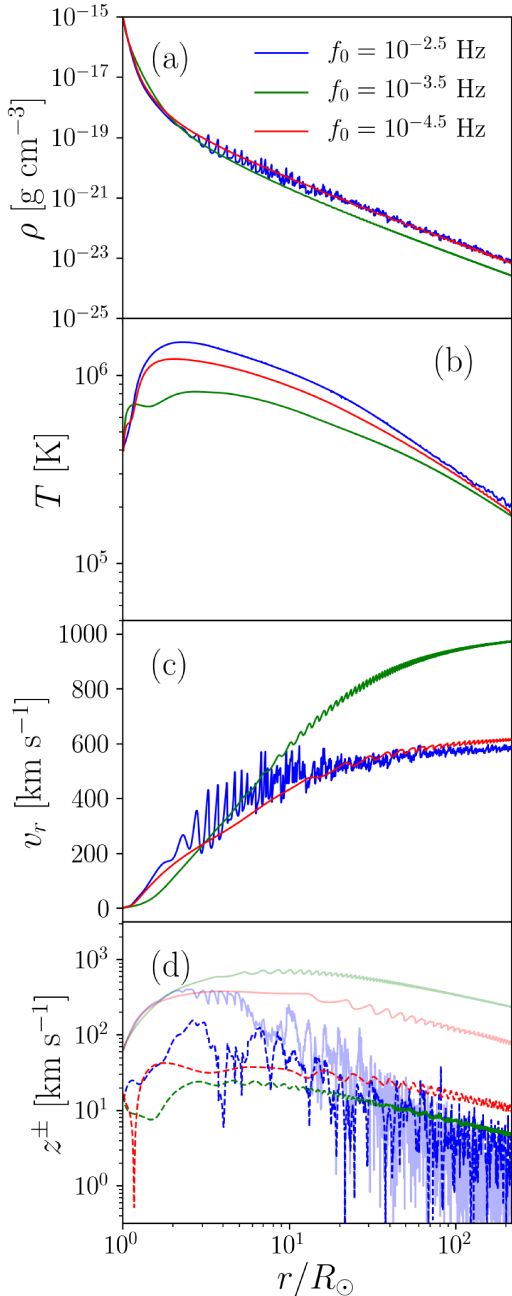


Figure 1. Snapshots of the quasi-steady states with different wave-injection frequencies. Blue, green and red lines indicate $f_0 = 10^{-2.5}$ Hz, $10^{-3.5}$ Hz, $10^{-4.5}$ Hz, respectively. Panels correspond to a: mass density, b: temperature, c: radial velocity, d: Elsässer variables. In Panel d, transparent and dashed lines indicate z^+ and z^- , respectively.

Although the same amount of energy flux ($F_0 = 8.4 \times 10^5$ erg cm $^{-3}$ s $^{-1}$) was injected in each case, the corresponding quasi-steady states showed different properties. Firstly, a significant density fluctuation is observed when $f_0 = 10^{-2.5}$ Hz. Because the large density fluctuation is attributed to PDI, it indicates that PDI can de-

velop only when $f_0 > 10^{-3.5}$ Hz. Elsässer variables also show evidence of PDI when $f_0 = 10^{-2.5}$ Hz. The ratio z^+/z^- is smaller than unity partly in $r/R_\odot > 50$ when $f_0 = 10^{-2.5}$ Hz, while $z^+/z^- \gg 1$ when $f_0 \lesssim 10^{-3.5}$ Hz. A natural interpretation of low z^+/z^- is that, as a result of PDI, a large amount of reflected Alfvén waves is generated (Sagdeev & Galeev 1969; Goldstein 1978; Suzuki & Inutsuka 2005) and is advected to 1 au. The coronal temperature is the lowest in the medium-frequency case ($f_0 = 10^{-3.5}$ Hz). When f_0 is high, because PDI occurs in the sub-Alfvénic corona, the coronal plasma is heated up by the shock and turbulence driven by PDI (Shoda et al. 2018). However, when f_0 is low, Alfvén waves reflect efficiently (An et al. 1990; Velli 1993; Cranmer & van Ballegooijen 2005) and the turbulence heating in the corona increases (Matthaeus et al. 1999; Dmitruk et al. 2002; Oughton et al. 2006). This is why the medium-frequency case, in which PDI does not occur and reflection is weak, shows the lowest temperature of the corona. As a result of the lower-temperature corona, the mass density of the wind is smaller and the wind is faster (Hansteen & Velli 2012).

In Figure 2, we show the dependence of solar wind parameters on f_0 . From left to right, we show the solar-wind velocity v_r at $r = 1$ au, maximum temperature T_{\max} , mass-loss rate $\dot{M} = \rho v_r 4\pi r^2$, and the sonic point r_* where the sound speed c_s is equal to the wind speed v_r . Here, we assumed $c_s = \sqrt{p/\rho}$ because the plasma is almost isothermal due to the strong thermal conduction near the sonic point. Every variable is averaged in time over 10^5 s.

Figure 2 shows that the solar wind properties depend non-monotonically on f_0 ; slow, high-temperature, and high-density winds are driven in the cases with high and low f_0 ; in contrast, fast, low-temperature, and low-density winds stream out in the cases with intermediate f_0 . As explained before, this bimodal behavior can be understood by the different characters of the reflection and dissipation of low- and high-frequency Alfvén waves; low-frequency waves dissipate by reflection-driven turbulence and high-frequency waves by PDI. In addition, Fig. 2 indicates that the corona and solar wind have a frequency-filtering mechanism; waves with a medium frequency $f_0 \sim 10^{-3.5}$ Hz are the least dissipative and most transparent in order to propagate through. This might be responsible for the dominance of the hour-scale Alfvén waves observed in the solar wind (Belcher & Davis 1971).

Some features found in Fig. 2 are consistent with previous research. In the high-frequency range, the solar wind velocity (Fig. 2a) decreases as f_0 increases, and this result is consistent with Ofman & Davila (1998),

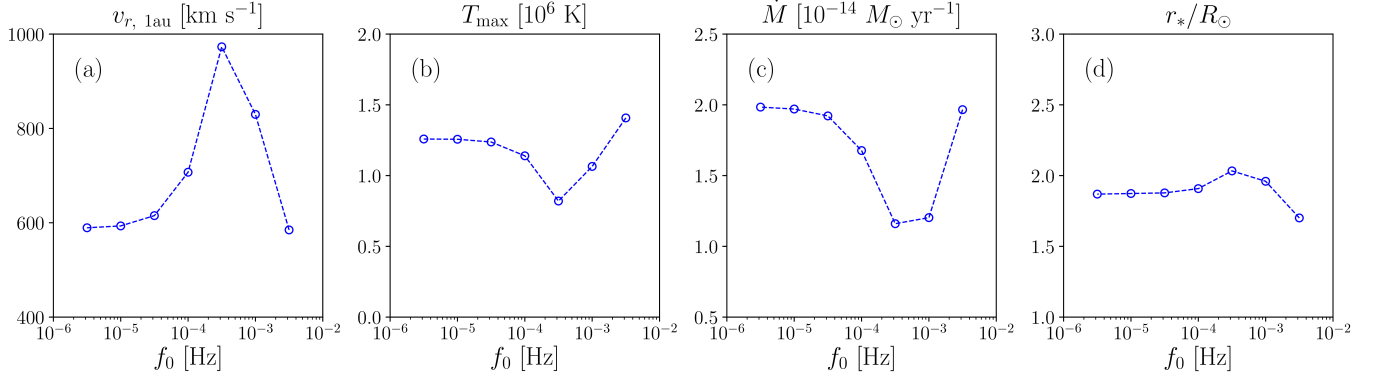


Figure 2. Parameters of the corona and solar wind as functions of wave-driving frequency. Panels indicate the a: solar wind speed at 1 au, b: maximum coronal temperature, c: mass-loss rate, and d: sonic point location. Each parameter is measured in the time-averaged quasi-steady states.

who showed the inverse correlation between the injection frequency and the resultant wind speed when $0.35 \text{ mHz} \lesssim f_0 \lesssim 3 \text{ mHz}$. The critical point r_* (Fig. 2d) has a negative correlation with the temperature. This is because the critical point is closer to the Sun when the sound speed is larger (Parker 1958).

3.2. Decay law of density fluctuation in the accelerating and expanding solar wind

Following Tenerani & Velli (2013), we derived the linear decay law for slow magnetoacoustic waves in the accelerating and expanding solar wind. We began with the conservation of mass: Eq. (4). Assuming that the density and radial velocity have mean ρ_0 , $v_{r,0}$ and small fluctuation $\delta\rho$, δv_r parts, we could express the linearized equation for $\delta\rho$ as

$$\frac{\partial}{\partial t} (\delta\rho S) + \frac{\partial}{\partial r} (\rho_0 \delta v_r S) + \frac{\partial}{\partial r} (\delta\rho v_{r,0} S) = 0. \quad (27)$$

where $S = r^2 f$ represents the cross section of flux tube.

We could safely assume that the compressible fluctuations come from upward slow mode because PDI generates the slow-mode wave propagating in the same direction as the parent Alfvén wave. Therefore, $\delta\rho$ and δv_r satisfy a characteristic relation of

$$\delta\rho/\rho_0 = \delta v_r/c_s. \quad (28)$$

This relation holds when the slow mode has acoustic nature. When $\beta \ll 1$, magnetic and acoustic perturbations decouple with each other. In addition, the gravity effect is negligible when the wavelength is much smaller than the scale height of stratification. Therefore, Eq. (28) is a good approximation because β is small and the scale height is large in and above the corona.

Combining Eq. (27) and Eq. (28), we had

$$\frac{\partial}{\partial t} (\delta\rho S) + \frac{\partial}{\partial r} [\delta\rho (v_{r,0} + c_s) S] = 0. \quad (29)$$

$\delta\rho$ was assumed to have following form:

$$\delta\rho \propto \exp[i(kr - \omega t)], \quad (30)$$

From Eqs. (27) and (30), we have

$$-i\omega + ik(c_s + v_{r,0}) + (v_{r,0} + c_s) \frac{\partial}{\partial r} \ln S + \frac{\partial}{\partial r} (v_{r,0} + c_s) = 0. \quad (31)$$

If the background has little variation and the third term in the left hand side is negligible, the usual dispersion relation of the acoustic wave ($\omega/k = c_s + v_{r,0}$) is obtained. If not, we have

$$\omega = (c_s + v_{r,0})k - i\gamma_{\text{acc}} - i\gamma_{\text{exp}}, \quad (32)$$

where

$$\gamma_{\text{acc}} = \frac{\partial}{\partial r} (v_{r,0} + c_s), \quad (33)$$

and

$$\gamma_{\text{exp}} = (v_{r,0} + c_s) \frac{\partial}{\partial r} \ln S, \quad (34)$$

are the damping rates by the acceleration and expansion of the solar wind, respectively. In the linear regime, the density fluctuations have decay rates of $\gamma_{\text{acc}} + \gamma_{\text{exp}}$.

Since density fluctuation should increase as a result of PDI, acceleration and expansion work to suppress the instability (Tenerani & Velli 2013; Del Zanna et al. 2015). The effective growth rate γ_{eff} of PDI is given as

$$\gamma_{\text{eff}} = \gamma_{\text{GD}} - \gamma_{\text{acc}} - \gamma_{\text{exp}}, \quad (35)$$

where γ_{GD} is a growth rate given by the Goldstein-Derby dispersion relation: Eq. (3).

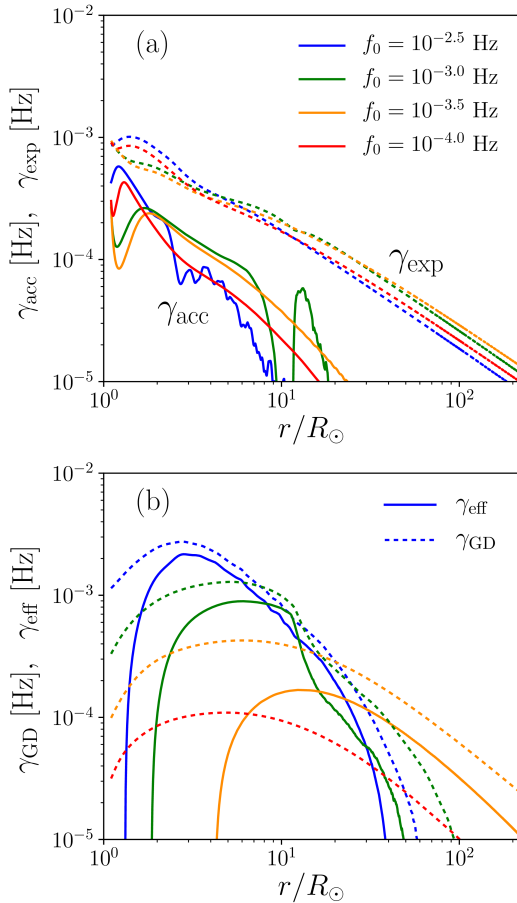


Figure 3. a: Decay rates of density fluctuation due to wind acceleration γ_{acc} (solid line) and due to wind expansion γ_{exp} (dashed line). b: Growth rate of PDI given by the Goldstein–Derby dispersion relation γ_{GD} (dashed line) and the effective growth rate γ_{eff} (solid line). Blue, green, orange, and red lines indicate $f_0 = 10^{-2.5}$ Hz, $10^{-3.0}$ Hz, $10^{-3.5}$ Hz, and $10^{-4.0}$ Hz, respectively. We note that γ_{eff} of $f_0 = 10^{-4.0}$ Hz (red solid) is negative in the entire region.

3.3. Doppler effect and effective growth rate

To discuss the possibility of the onset of PDI for each f_0 , we calculated γ_{eff} using Eq. (35). The normalized growth rate $\gamma_{\text{GD}}/\omega$ was calculated from Eq. (3). We should note that $\omega \neq 2\pi f_0$ because of the Doppler effect by the acceleration of the solar wind. ω should be the intrinsic frequency, that is, the wave frequency observed in a co-moving frame of the solar wind. Because the wave frequency observed from a fixed coordinate is constant in a quasi-steady state, the wave number $k(r)$ satisfies

$$k(r) = \frac{2\pi f_0}{v_A(r) + v_r(r)}. \quad (36)$$

When we observed this wave in a co-moving frame, the wave number was invariant and the phase speed de-

creased to $v_A(r)$, and therefore,

$$\omega = v_A(r)k(r) = 2\pi f_0 \frac{v_A(r)}{v_A(r) + v_r(r)}. \quad (37)$$

This means that the intrinsic frequency decreases in an accelerating flow. In the accelerating expanding box model, this effect is mentioned as the box-stretching effect (Tenerani & Velli 2017). A similar argument appears in deriving the wave-action conservation (Dewar 1970; Heinemann & Olbert 1980).

We should note that, the wind-acceleration effect appears in different ways. As discussed in Section 3.2, the wind acceleration works to reduce the density fluctuation. In addition, as discussed here, wind acceleration also causes the Doppler effect.

In Figure 3, we show γ_{eff} , γ_{GD} , γ_{acc} , and γ_{exp} as functions of height to see the effects of wind acceleration and expansion on the growth rate of PDI. γ_{acc} (solid lines) and γ_{exp} (dashed lines) are shown in Figure 3a, while γ_{eff} and γ_{GD} are shown in Figure 3b. The colors represent the injection frequency as follows: $f_0 = 10^{-2.5}$ Hz (blue), $f_0 = 10^{-3.0}$ Hz (green), $f_0 = 10^{-3.5}$ Hz (orange), and $f_0 = 10^{-4.0}$ Hz (red). Figure 3a shows that the expansion (γ_{exp}) dominates the acceleration (γ_{acc}) in the damping of the PDI. As a result, γ_{GD} is reduced to γ_{eff} . The reduction factors, $\gamma_{\text{acc}}/\gamma_{\text{GD}}$ and $\gamma_{\text{exp}}/\gamma_{\text{GD}}$, are larger for smaller injection frequencies, f_0 , because γ_{GD} is proportional to f_0 . Specifically when $f_0 = 10^{-4.0}$ Hz, γ_{GD} is smaller than the reduction factor, $\gamma_{\text{acc}} + \gamma_{\text{exp}}$, and the effective growth rate is negative. The local maxima of γ_{GD} is determined by the balance between plasma beta and wave amplitude (see Eq. (1)); the plasma beta is low and the wave amplitude is small in the lower corona and vice versa in the distant solar wind.

3.4. Onset and suppression of PDI

To discuss the threshold of the onset of PDI, we calculated the maximum fractional density fluctuation n_{max} and the normalized cross-helicity (Alfvénicity) σ_c at 1 au. Here we defined n_{max} and σ_c as

$$n_{\text{max}} = \max \left(\frac{1}{\rho_{\text{ave}}} \sqrt{\langle (\rho - \rho_{\text{ave}})^2 \rangle} \right), \quad \rho_{\text{ave}} = \langle \rho \rangle, \quad (38)$$

$$\sigma_c = \frac{\langle z^+ \rangle^2 - \langle z^- \rangle^2}{\langle z^+ \rangle^2 + \langle z^- \rangle^2}, \quad (39)$$

where $\langle X \rangle$ denotes the time-averaged value of X and $\max(X)$ denotes the maximum value of X in space. We note that the sign of σ_c is opposite to the sign of $H_c = \mathbf{v} \cdot \mathbf{B}$. These values can be useful indicators of PDI because PDI generates large-amplitude density fluctuation, which increases n , and back-scattered

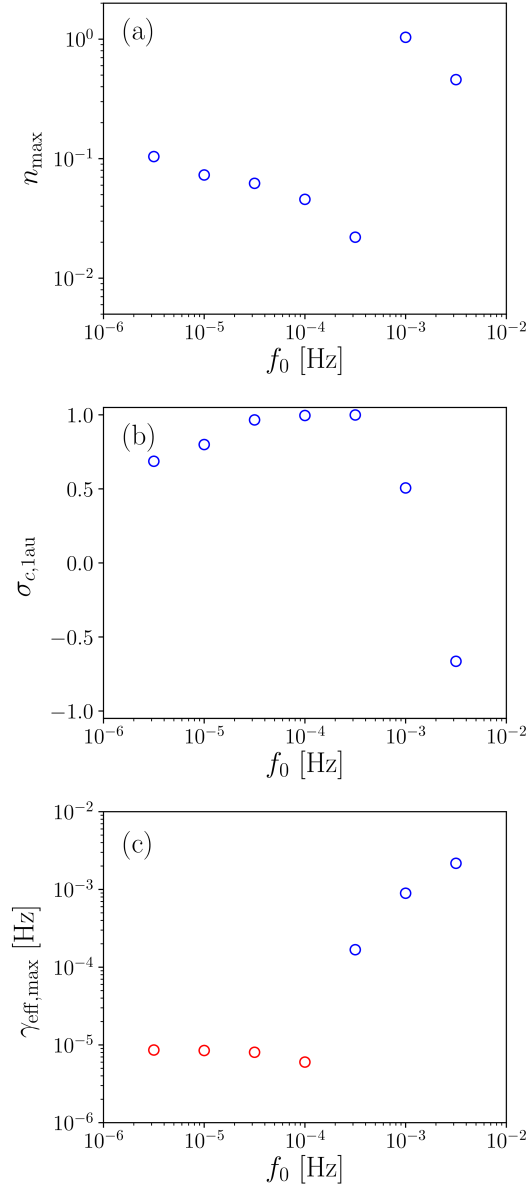


Figure 4. Solar wind parameters versus wave-injection frequency f_0 . Each panel indicates a: maximum fractional density fluctuation n , b: normalized cross-helicity σ_c at 1 au, c: maximum effective growth rate γ_{eff} (blue: positive, red: negative).

Alfvén waves, which reduce σ_c . The latter effect works to reduce σ_c . According to Cranmer & van Ballegoijen (2012), without PDI, $\delta\rho_{\text{rms}}/\rho_0 \lesssim 0.1$, and thus $\delta\rho_{\text{rms}}/\rho_0 > 0.1$ indicates the PDI.

In Figure 4, we show a: n_{\max} , b: σ_c at 1 au, and c: the maximum effective growth rate $\gamma_{\text{eff,max}}$ (blue: positive, red: negative) as functions of f_0 . When $f_0 \lesssim 10^{-3.5}$ Hz, both n_{\max} and σ_c show monotonic trends with f_0 : n_{\max} decreases and σ_c increases as f_0 increases. This is explained as follows. As f_0 becomes smaller, Alfvén waves

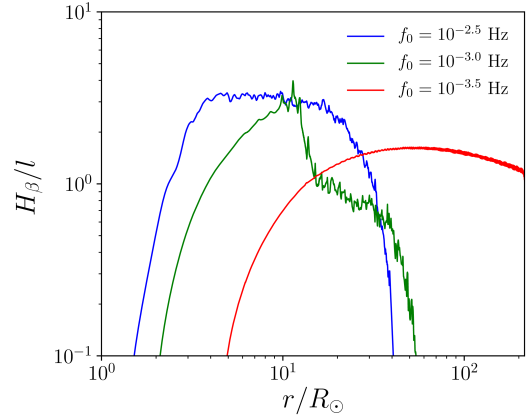


Figure 5. Scale ratio H_β/l where l and H_β denote the typical propagation length scale during the PDI growth and the scale length of plasma beta, respectively. Blue, green, and red lines indicate $f_0 = 10^{-2.5}$ Hz, $10^{-3.0}$ Hz, and $10^{-3.5}$ Hz, respectively.

are reflected more efficiently (Ferraro & Plumpton 1958; An et al. 1990; Velli 1993; Cranmer & van Ballegoijen 2005; Hollweg & Isenberg 2007). If Alfvén waves are reflected in the solar wind beyond the Alfvén point, reflected Alfvén waves are advected towards 1 au and contribute to reducing σ_c . Note that the inward waves vanish near the Alfvén point (Verdini et al. 2009; Tenerani & Velli 2017). When the amount of reflected Alfvén waves increases, the interaction between outward and inward waves is activated. This wave-wave collision excites not only turbulence (Iroshnikov 1964; Kraichnan 1965; Dobrowolny et al. 1980; Goldreich & Sridhar 1995), but also the slow-mode generation (Wentzel 1974; Uchida & Kaburaki 1974) by the modulation of magnetic field pressure (Hollweg 1971; Kudoh & Shibata 1999; Cranmer & Woolsey 2015). Magnetic field modulation also leads to direct steepening to fast shock (Cohen & Kulsrud 1974; Kennel et al. 1990; Suzuki 2004). Owing to these processes, larger-density fluctuation is likely to be generated in the presence of larger-amplitude reflected Alfvén waves.

The monotonic trend in $10^{-5.5}$ Hz $\lesssim f_0 \lesssim 10^{-3.5}$ Hz breaks down near $f_0 \approx 10^{-3}$ Hz. When f_0 gets larger than 10^{-3} Hz, n_{\max} becomes larger than 0.1 and σ_c becomes smaller than 0.5. Considering the fact that PDI generates large amounts of density fluctuation and reflected Alfvén waves, Figure 4 indicates that the frequency threshold of the onset of PDI is $10^{-3.5}$ Hz $< f_0 < 10^{-3}$ Hz. This means that, even though $\gamma_{\text{eff,max}}$ is positive when $f_0 = 10^{-3.5}$ Hz, PDI cannot develop with this injection frequency. Tenerani & Velli (2013) argued that PDI is suppressed not only by the acceleration and expansion of the solar wind but also by the

inhomogeneity of the solar wind, because the resonance condition changes as the plasma parameters such as the plasma beta, Alfvén speed and wave amplitude, vary. In Figure 5, we show the ratio between the propagation length during growth time l and the scale length of the plasma beta (H_β):

$$l = \frac{v_A + v_r}{\gamma_{\text{eff}}}, \quad H_\beta = \left| \frac{\beta}{\partial\beta/\partial r} \right|. \quad (40)$$

The ratio, H_β/l , can be used as a measure of how the inhomogeneity of the background field affects the onset of PDI; if H_β/l is small $\lesssim 1$, the background inhomogeneity could suppress the PDI. Figure 5 shows H_β/l versus height. This indicates that, when $f_0 = 10^{-3.5}$ Hz, PDI cannot evolve because the scale ratio H_β/l is at most around unity and the inhomogeneity affects the growth of PDI.

Another possible reason that PDI is not observed when $f_0 = 10^{-3.5}$ Hz is that the typical growth time is too small to develop before 1 au. γ_{eff} averaged over the entire simulation box is approximately $\bar{\gamma}_{\text{eff}} = 5 \times 10^{-5}$ Hz, corresponding to the timescale of $\bar{\tau} = 2 \times 10^4$ s. Therefore, because it takes a few $\bar{\tau}$ to reach the saturation phase of PDI, the evolution timescale ($\sim 10^5$ s) is comparable to the propagation timescale up to 1 au ($\sim 2 \times 10^5$ s). This indicates that 1 au might be too short for the PDI of $f_0 = 10^{-3.5}$ Hz to develop.

4. BROADBAND-WAVE INJECTION

Next, we applied the broadband-wave injection to discuss the consistency with observation. The boundary condition is given as

$$z_{x,y}^+ = \int_{f_{\text{min}}}^{f_{\text{max}}} P(f) \sin(2\pi ft + \phi_{x,y}(f)) df, \quad (41)$$

where $P(f)$ is determined so that the root-mean-square value is $2v_{\text{rms},0}$ and the power show $1/f$ spectrum in $f_{\text{min}} \leq f \leq f_{\text{max}}$ (Bruno & Carbone 2013). $\phi_{x,y}(f)$ are random functions of f . We fixed $f_{\text{max}} = 10^{-2}$ Hz, corresponding to 100 s in terms of period. Note that some observations show an even higher frequency component (He et al. 2009; Okamoto & De Pontieu 2011; Shoda & Yokoyama 2018). f_{min} is the free parameter. In this study, we calculated three cases: $f_{\text{min}} = 10^{-3}$ Hz, 10^{-4} Hz, 10^{-5} Hz, each of which corresponded to the largest timescale of the photospheric transverse motion (Matsumoto & Kitai 2010), the coronal transverse motion (Morton et al. 2015), and the solar-wind fluctuations (Tu & Marsch 1995), respectively.

4.1. Quasi-steady state

As in Section 3, we begin by discussing the quasi-steady states. Figure 6 shows the same variables as those shown in Figure 1 except for Panel d, where the transverse velocity v_\perp is shown instead of the Elsässer variables. Color represents $f_{\text{min}} = 10^{-3}$ Hz (blue), 10^{-4} Hz (green), 10^{-5} Hz (red), respectively. Because the main motivation of broadband-wave injection is to compare to observations, we also show several observational values. In Panel a, we show the density observation by Wilhelm et al. (1998) (circles) and Lamy et al. (1997) (stars). In converting the observed electron density n_e to mass density ρ , we simply assumed $\rho = m_p n_e$. In Panel b, circles and stars correspond to the results from Landi (2008) and Cranmer (2004, 2009), respectively. In Panel c, observed ion-outflow velocity is plotted by stars (Zangrilli et al. 2002), while the results of IPS observation are indicated by crosses (Kojima et al. 2004).

4.2. Density fluctuation

The density fluctuation in the solar wind is observed by radio-wave observation. As explained in the Introduction, density fluctuation possibly plays a role in reflecting Alfvén waves in the corona and solar wind (van Ballegooijen & Asgari-Targhi 2016).

When we applied the broadband-wave injection, it was difficult to obtain the amplitude of the density fluctuation that was solely attributed to PDI, because the density fluctuates not only by PDI but also by the time variation of the injected energy flux. Since the density fluctuation that comes from the injection has a timescale of typically f_{min} , in this study, we defined the density fluctuation as high-frequency ($> f_{\text{min}}$) components. Given that we have density $\rho(r, t)$, the fractional fluctuation $n_f(r)$ is given as

$$n_f(r) = \frac{1}{\rho_{\text{ave}}} \sqrt{\frac{1}{2\pi\tau_0} \int_{|\omega| > 2\pi f_{\text{th}}} |\tilde{\rho}(r, \omega)|^2 d\omega}, \quad (42)$$

where

$$\tilde{\rho}(r, \omega) = \int_0^{\tau_0} dt \rho(r, t) e^{i\omega t}. \quad (43)$$

Note that Parseval's identity holds as follows:

$$\int dt |\rho(r, t)|^2 = \frac{1}{2\pi} \int d\omega |\tilde{\rho}(r, \omega)|^2. \quad (44)$$

f_{th} is the frequency threshold. Here, we set $f_{\text{th}} = 10^{-3}$ Hz. Although this value was a rather arbitrary choice, we confirmed that the radial trend of n_f does not depend on f_{th} .

Figure 7 shows the radial profiles of $n_f(r)$. Rectangles are observational values taken from Cranmer & van

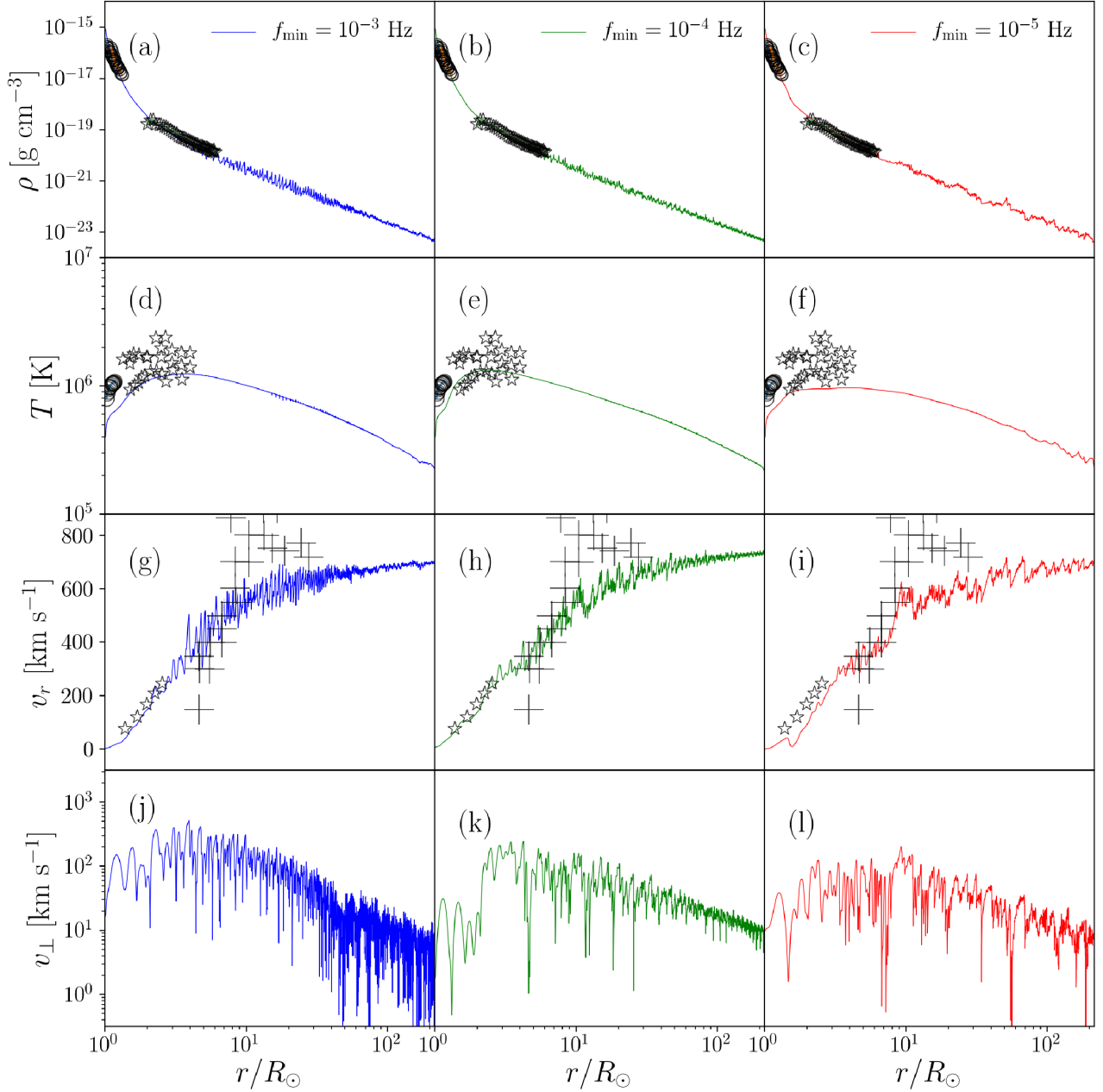


Figure 6. Quasi-steady states with different f_{\min} values. Blue, green and red lines indicate $f_{\min} = 10^{-3}$ Hz, 10^{-4} Hz, 10^{-5} Hz, respectively. a-c: mass density. Shown by circles and stars are observations by Wilhelm et al. (1998) and by Lamy et al. (1997), respectively. d-f: temperature. Shown by circles and stars are observations by Landi (2008) and compilation of observed data by Cranmer (2004, 2009), respectively. g-i: radial velocity. Shown by stars are ion outflow speed by Zangrilli et al. (2002), while the crosses represent the IPS observations (Kojima et al. 2004). j-l: transverse velocity (Alfvén-wave amplitude).

Ballegooijen (2012). The rectangle near $r = 5R_{\odot}$ indicates the radio sounding data (Coles & Harmon 1989; Spangler 2002; Harmon & Coles 2005) while the rectangles in $r \gtrsim 100R_{\odot}$ indicate the in-situ data by Marsch & Tu (1990). The circles indicate the observation by Miyamoto et al. (2014).

Our three cases nicely explain the overall radial profile of the observed density fluctuation peaked at $r \sim 5 -$

$10R_{\odot}$ (Miyamoto et al. 2014). The peak of n_f in our calculation is created by the high-frequency ($f > 10^{-3.5}$ Hz) Alfvén waves that are subject to PDI (Fig.3b). The largest effective growth rate γ_{eff} is peaked in $r \sim 2 - 10R_{\odot}$ when the parent-wave frequency is $10^{-3} - 10^{-2}$ Hz. Therefore, the large density fluctuations are excited as an outcome of the PDI in these locations. To summarize, the observed density fluctuation is ex-

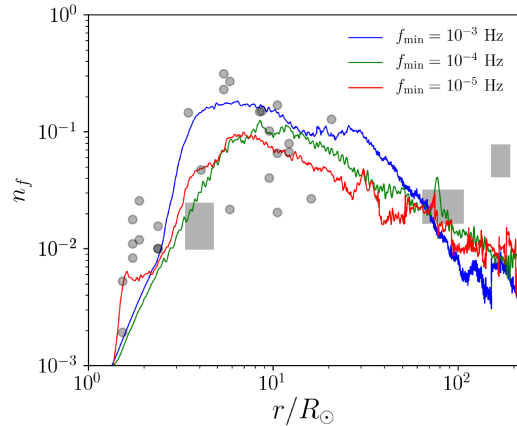


Figure 7. Fractional density fluctuation n_f versus heliocentric distance. Blue, green and red lines indicate $f_{\min} = 10^{-3}$ Hz, 10^{-4} Hz, 10^{-5} Hz, respectively. Shown by gray rectangles and circles are the observational values (see text).

plained by the evolution of the PDI of high-frequency ($10^{-2} - 10^{-3}$ Hz) Alfvén waves.

4.3. Cross-helicity in the solar wind

Because the radial evolution of Elsässer variables z^\pm in the heliosphere has been observed (Bavassano et al. 1982, 2000), we can test our theoretical model by comparison with these observations. In Figure 8, we show the radial profile of time-averaged Elsässer variables (z^+ : solid line, z^- : dashed line) with different f_{\min} values ($f_{\min} = 10^{-3}$ Hz: blue, 10^{-4} Hz: green, 10^{-5} Hz: red). Also shown by gray transparent lines are the observational trends by Bavassano et al. (2000).

While z^+ is consistent with observation when $f_{\min} = 10^{-4}$, 10^{-5} Hz, we have a much smaller z^+ compared with observation when $f_{\min} = 10^{-3}$ Hz. Because PDI evolves when $f_0 \gtrsim 10^{-3}$ Hz, this discrepancy indicates that, via PDI, excessive energy transfer from z^+ to z^- occurs. When f_{\min} becomes smaller, the intensity of high-frequency waves that are subject to PDI is reduced because the total wave power is fixed. This is why the signature of PDI is weak for smaller f_0 . Our result indicates that the cross-helicity evolution in the solar wind is dominated by the linear reflection (Zhou & Matthaeus 1990; Velli et al. 1991; Verdini & Velli 2007). Because the simulated z^- approaches the observational value as f_{\min} decreases, as a result of PDI suppression, the cross-helicity evolution in the solar wind is governed by linear reflection of low-frequency ($f_0 \sim 10^{-5}$ Hz) components.

5. SUMMARY & DISCUSSION

In this study, using numerical simulations, we investigated the threshold of the onset of PDI by changing the Alfvén-wave injection. As discovered by Ten-

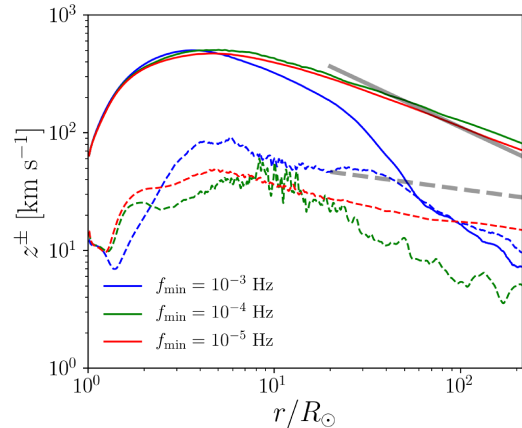


Figure 8. Radial profiles of time-averaged Elsässer variables. Solid and dashed lines indicate z^+ (anti-sunward) and z^- (sunward) components. Blue, green and red lines indicate $f_{\min} = 10^{-3}$ Hz, 10^{-4} Hz, 10^{-5} Hz, respectively. Also shown by gray lines are observational trends by Bavassano et al. (2000).

erani & Velli (2013) and Del Zanna et al. (2015), wind acceleration and expansion work to reduce the growth rate of PDI. We have solved the wave propagation self-consistently from the coronal base to 1 au, and this was then compared with the accelerating expanding box simulation.

Firstly, we investigated the fundamental processes of PDI by applying monotonic-wave injection with frequency f_0 . Our results show that PDI can develop when $f_0 \gtrsim 10^{-3}$ Hz, while we observe no signature of PDI when $f_0 \lesssim 10^{-3.5}$ Hz. Owing to the wind acceleration and expansion, the growth rate of PDI becomes negative when $f_0 \lesssim 10^{-4.0}$ Hz. When $f_0 \lesssim 10^{-3.5}$ Hz, even though the growth rate of PDI is positive, PDI cannot develop. The suppression by solar wind inhomogeneity or the long timescale of growth might be the reason for this.

The frequency-filtering mechanism can operate in the corona and solar wind due to the bimodal behavior of wave dissipation with respect to frequency. The low-frequency ($f_0 \lesssim 10^{-4}$ Hz) waves undergo linear reflection and generate Alfvénic turbulence from the interaction with counter-propagating waves. The high-frequency ($f_0 \gtrsim 10^{-3}$ Hz) waves dissipate through the PDI. As a result of the efficient heating, dense, hot and relatively slow winds are driven in the cases with $f_0 \lesssim 10^{-4}$ Hz or $f_0 \gtrsim 10^{-3}$ Hz. In contrast, the intermediate-frequency ($f_0 \approx 10^{-3.5}$ Hz) waves are not severely subjected to these damping mechanisms. As a result, fast and less dense wind emanates from the relatively cool corona in this case. This indicates that the corona and solar wind have a frequency-filtering effect of

the Alfvén wave, and as a result, the medium-frequency wave is likely to permeate. This is a possible reason for the hour-scale waves observed in the solar wind (Belcher & Davis 1971).

Secondly, we applied broadband-wave injection to compare the numerical results with observation. The observed radial trend of the density fluctuation can be well explained by the evolution of the high-frequency ($f_0 \gtrsim 10^{-3}$ Hz) Alfvén waves. However, the observed trend of the cross-helicity can be explained by the linear reflection of the low-frequency ($f_0 < 10^{-4}$ Hz) Alfvén waves. These results show that the Alfvén waves in a wide range of frequency play an essential role in the global solar wind.

There are several limitations in our model. The most severe limitation is the treatment of turbulence. We have applied a simple one-point-closure model of Alfvén wave turbulence (Eq. (12) and (13)) with the correlation length that increases with an expanding flux tube (Eq. (15)). However, Cranmer & van Ballegooijen (2012) showed that Eq. (15) possibly underestimates the correlation length. To overcome this, we needed to solve the transport equation of λ (Breech et al. 2008; Usmanov et al. 2011). In addition, the correlation length should be different between z^+ and z^- (Zank et al. 2017; Shiota et al. 2017). More sophisticated treatment of the turbulence, including the shell model (Buchlin & Velli 2007; Verdini et al. 2012), remains as a future work.

Another limitation is one-dimensional modeling. While the Alfvén wave turbulence is taken into account phenomenologically, we completely ignore the effect of phase mixing (Heyvaerts & Priest 1983; Kaneko et al. 2015; Antolin et al. 2015; Okamoto et al. 2015) by 1D modeling. Besides, it has been shown by Del Zanna et al. (2001) that the onset (and possibly growth) of parametric decay instability is slower in 3D than in 1D. Our quantitative discussion might be slightly modified by the 1D assumption. Also, we cannot take into account the wave refraction in the lower region (Rosenthal et al. 2002; Bogdan et al. 2003). In future, we need to conduct a 3D MHD simulation for the reasons above.

In this study, we have focused on the frequency dependence. Since the growth rate of parametric decay

instability depends also on plasma beta and wave amplitude (Goldstein 1978; Derby 1978). Suzuki & Inutsuka (2006) investigated the dependence on the injected wave amplitude. Readers probably expect that the PDI is suppressed for smaller wave injection according to Eq. (1). However, the response of the solar wind totally changes the situation. A case with smaller injection gives lower coronal temperature because of the suppressed heating. As a result, the plasma beta in the corona is lower, and larger density fluctuations are excited by more activated PDI as shown in Figure 9 of Suzuki & Inutsuka (2006). Similarly, it is expected that the density variation is large when the magnetic field is stronger and the plasma beta is lower.

There are also ambiguities in the thermal flux in the free-streaming regime. We chose $\alpha = 2$ in evaluating the magnitude of free-streaming thermal flux. Although $\alpha = 4$ has been sometimes used (Leer et al. 1982; Withbroe 1988; Landi & Pantellini 2003; Cranmer et al. 2007; van Ballegooijen & Asgari-Targhi 2016), $\alpha = 4$ might overestimate the actual flux because thermal conduction can be suppressed by the local instability and turbulence (Gary et al. 1999; Roberg-Clark et al. 2017; Komarov et al. 2017; Tong et al. 2018). Indeed Cranmer et al. (2009) showed that $\alpha = 1.05$ yields good agreement with observation, and several recent studies used $\alpha = 1.05$ (Usmanov et al. 2011; van der Holst et al. 2014). The precise value of α should depend on the solar wind condition. Since the change in α does not strongly affect the physical quantities of the solar wind (Cranmer et al. 2007), we expect that our findings are independent on α .

M.S. is supported by the Leading Graduate Course for Frontiers of Mathematical Sciences and Physics (FMSP) and Grant-in-Aid for Japan Society for the Promotion of Science (JSPS) Fellows. T.Y. is supported by JSPS KAKENHI Grant Number 15H03640. T.K.S. is supported in part by Grants-in-Aid for Scientific Research from the MEXT of Japan, 17H01105. Numerical calculations were in part carried out on the PC cluster at the Center for Computational Astrophysics, National Astronomical Observatory of Japan.

REFERENCES

- Alfvén, H. 1942, *Nature*, 150, 405
- . 1947, *MNRAS*, 107, 211
- An, C.-H., Suess, S. T., Moore, R. L., & Musielak, Z. E. 1990, *ApJ*, 350, 309
- Antolin, P., Okamoto, T. J., De Pontieu, B., Uitenbroek, H., Van Doorselaere, T., & Yokoyama, T. 2015, *ApJ*, 809, 72
- Arge, C. N., & Pizzo, V. J. 2000, *J. Geophys. Res.*, 105, 10465

- Banerjee, D., Pérez-Suárez, D., & Doyle, J. G. 2009, *A&A*, 501, L15
- Bavassano, B., Dobrowolny, M., Mariani, F., & Ness, N. F. 1982, *J. Geophys. Res.*, 87, 3617
- Bavassano, B., Pietropaolo, E., & Bruno, R. 2000, *J. Geophys. Res.*, 105, 15959
- Belcher, J. W. 1971, *ApJ*, 168, 509
- Belcher, J. W., & Davis, Jr., L. 1971, *J. Geophys. Res.*, 76, 3534
- Bogdan, T. J., et al. 2003, *ApJ*, 599, 626
- Bourdin, P.-A. 2017, *ApJL*, 850, L29
- Bowen, T. A., Badman, S., Hellinger, P., & Bale, S. D. 2018, *ApJL*, 854, L33
- Breech, B., Matthaeus, W. H., Minnie, J., Bieber, J. W., Oughton, S., Smith, C. W., & Isenberg, P. A. 2008, *Journal of Geophysical Research (Space Physics)*, 113, A08105
- Bruno, R., & Carbone, V. 2013, *Living Reviews in Solar Physics*, 10, 2
- Buchlin, E., & Velli, M. 2007, *ApJ*, 662, 701
- Chandran, B. D. G. 2018, *Journal of Plasma Physics*, 84, 905840106
- Chandran, B. D. G., & Hollweg, J. V. 2009, *ApJ*, 707, 1659
- Cohen, R. H., & Dewar, R. L. 1974, *J. Geophys. Res.*, 79, 4174
- Cohen, R. H., & Kulsrud, R. M. 1974, *Physics of Fluids*, 17, 2215
- Coleman, Jr., P. J. 1968, *ApJ*, 153, 371
- Coles, W. A., & Harmon, J. K. 1989, *ApJ*, 337, 1023
- Cranmer, S. R. 2004, in *ESA Special Publication*, Vol. 575, *SOHO 15 Coronal Heating*, ed. R. W. Walsh, J. Ireland, D. Danesy, & B. Fleck, 154
- Cranmer, S. R. 2009, *Living Reviews in Solar Physics*, 6, 3
- Cranmer, S. R., Matthaeus, W. H., Breech, B. A., & Kasper, J. C. 2009, *ApJ*, 702, 1604
- Cranmer, S. R., & van Ballegoijen, A. A. 2005, *ApJS*, 156, 265
- . 2012, *ApJ*, 754, 92
- Cranmer, S. R., van Ballegoijen, A. A., & Edgar, R. J. 2007, *ApJS*, 171, 520
- Cranmer, S. R., & Woolsey, L. N. 2015, *ApJ*, 812, 71
- De Groof, A., & Goossens, M. 2002, *A&A*, 386, 691
- De Pontieu, B., et al. 2007, *Science*, 318, 1574
- Del Zanna, L., Matteini, L., Landi, S., Verdini, A., & Velli, M. 2015, *Journal of Plasma Physics*, 81, 325810102
- Del Zanna, L., Velli, M., & Londrillo, P. 2001, *A&A*, 367, 705
- Derby, Jr., N. F. 1978, *ApJ*, 224, 1013
- Dewar, R. L. 1970, *Physics of Fluids*, 13, 2710
- Dmitruk, P., & Matthaeus, W. H. 2003, *ApJ*, 597, 1097
- Dmitruk, P., Matthaeus, W. H., Milano, L. J., Oughton, S., Zank, G. P., & Mullan, D. J. 2002, *ApJ*, 575, 571
- Dobrowolny, M., Mangeney, A., & Veltri, P. 1980, *Physical Review Letters*, 45, 144
- Dorfman, S., & Carter, T. A. 2016, *Physical Review Letters*, 116, 195002
- Elsässer, W. M. 1950, *Physical Review*, 79, 183
- Ferraro, C. A., & Plumpton, C. 1958, *ApJ*, 127, 459
- Fu, X., Li, H., Guo, F., Li, X., & Roytershteyn, V. 2017, *ArXiv e-prints*
- Fujiki, K., Tokumaru, M., Iju, T., Hakamada, K., & Kojima, M. 2015, *SoPh*, 290, 2491
- Galeev, A. A., & Oraevskii, V. N. 1963, *Soviet Physics Doklady*, 7, 988
- Gary, G. A. 2001, *SoPh*, 203, 71
- Gary, S. P., Neagu, E., Skoug, R. M., & Goldstein, B. E. 1999, *J. Geophys. Res.*, 104, 19843
- Ghosh, S., & Goldstein, M. L. 1994, *J. Geophys. Res.*, 99, 13
- Ghosh, S., Vinas, A. F., & Goldstein, M. L. 1994, *J. Geophys. Res.*, 99, 19
- Goldreich, P., & Sridhar, S. 1995, *ApJ*, 438, 763
- Goldstein, M. L. 1978, *ApJ*, 219, 700
- Goossens, M., Andries, J., Soler, R., Van Doorselaere, T., Arregui, I., & Terradas, J. 2012, *ApJ*, 753, 111
- Grappin, R., & Velli, M. 1996, *J. Geophys. Res.*, 101, 425
- Grappin, R., Velli, M., & Mangeney, A. 1993, *Physical Review Letters*, 70, 2190
- Hahn, M., & Savin, D. W. 2013, *ApJ*, 776, 78
- Hansteen, V. H., & Velli, M. 2012, *SSRv*, 172, 89
- Harmon, J. K., & Coles, W. A. 2005, *Journal of Geophysical Research (Space Physics)*, 110, A03101
- He, J.-S., Tu, C.-Y., Marsch, E., Guo, L.-J., Yao, S., & Tian, H. 2009, *A&A*, 497, 525
- Heinemann, M., & Olbert, S. 1980, *J. Geophys. Res.*, 85, 1311
- Heyvaerts, J., & Priest, E. R. 1983, *A&A*, 117, 220
- Hollweg, J. V. 1971, *J. Geophys. Res.*, 76, 5155
- . 1974, *J. Geophys. Res.*, 79, 3845
- . 1976, *J. Geophys. Res.*, 81, 1649
- Hollweg, J. V., Bird, M. K., Volland, H., Edenhofer, P., Stelzried, C. T., & Seidel, B. L. 1982, *J. Geophys. Res.*, 87, 1
- Hollweg, J. V., Cranmer, S. R., & Chandran, B. D. G. 2010, *ApJ*, 722, 1495
- Hollweg, J. V., & Isenberg, P. A. 2007, *Journal of Geophysical Research (Space Physics)*, 112, 8102
- Hoshino, M., & Goldstein, M. L. 1989, *Physics of Fluids B*, 1, 1405

- Hossain, M., Gray, P. C., Pontius, Jr., D. H., Matthaeus, W. H., & Oughton, S. 1995, *Physics of Fluids*, 7, 2886
- Iroshnikov, P. S. 1964, *Soviet Ast.*, 7, 566
- Iwai, K., Shibasaki, K., Nozawa, S., Takahashi, T., Sawada, S., Kitagawa, J., Miyawaki, S., & Kashiwagi, H. 2014, *Earth, Planets, and Space*, 66, 149
- Jacques, S. A. 1977, *ApJ*, 215, 942
- Jayanti, V., & Hollweg, J. V. 1993, *J. Geophys. Res.*, 98, 19
- Kaneko, T., Goossens, M., Soler, R., Terradas, J., Van Doorselaere, T., Yokoyama, T., & Wright, A. N. 2015, *ApJ*, 812, 121
- Kennel, C. F., Blandford, R. D., & Wu, C. C. 1990, *Physics of Fluids B*, 2, 253
- Kojima, M., Breen, A. R., Fujiki, K., Hayashi, K., Ohmi, T., & Tokumaru, M. 2004, *Journal of Geophysical Research (Space Physics)*, 109, A04103
- Komarov, S., Schekochihin, A., Churazov, E., & Spitkovsky, A. 2017, *ArXiv e-prints*
- Kopp, R. A., & Holzer, T. E. 1976, *SoPh*, 49, 43
- Kraichnan, R. H. 1965, *Physics of Fluids*, 8, 1385
- Kudoh, T., & Shibata, K. 1999, *ApJ*, 514, 493
- Lamy, P., Quémenerais, E., Llebaria, A., Bout, M., Howard, R., Schwenn, R., & Simnett, G. 1997, in *ESA Special Publication, Vol. 404, Fifth SOHO Workshop: The Corona and Solar Wind Near Minimum Activity*, ed. A. Wilson, 491
- Landi, E. 2008, *ApJ*, 685, 1270
- Landi, S., & Pantellini, F. 2003, *A&A*, 400, 769
- Lashmore-Davies, C. N. 1976, *Physics of Fluids*, 19, 587
- Leer, E., Holzer, T. E., & Fla, T. 1982, *SSRv*, 33, 161
- Levine, R. H., Altschuler, M. D., Harvey, J. W., & Jackson, B. V. 1977, *ApJ*, 215, 636
- Lionello, R., Velli, M., Downs, C., Linker, J. A., Mikić, Z., & Verdini, A. 2014, *ApJ*, 784, 120
- Magyar, N., Van Doorselaere, T., & Goossens, M. 2017, *Scientific Reports*, 7, 14820
- Malara, F., Primavera, L., & Veltri, P. 2000, *Physics of Plasmas*, 7, 2866
- Malara, F., & Velli, M. 1996, *Physics of Plasmas*, 3, 4427
- Marsch, E., & Tu, C.-Y. 1990, *J. Geophys. Res.*, 95, 11945
- Matsumoto, T., & Kitai, R. 2010, *ApJL*, 716, L19
- Matsumoto, T., & Suzuki, T. K. 2012, *ApJ*, 749, 8
- . 2014, *MNRAS*, 440, 971
- Matthaeus, W. H., Zank, G. P., Oughton, S., Mullan, D. J., & Dmitruk, P. 1999, *ApJL*, 523, L93
- McIntosh, S. W., de Pontieu, B., Carlsson, M., Hansteen, V., Boerner, P., & Goossens, M. 2011, *Nature*, 475, 477
- Miyamoto, M., et al. 2014, *ApJ*, 797, 51
- Miyoshi, T., & Kusano, K. 2005, *Journal of Computational Physics*, 208, 315
- Morton, R. J., Tomczyk, S., & Pinto, R. 2015, *Nature Communications*, 6, 7813
- Nariyuki, Y., Matsukiyo, S., & Hada, T. 2008, *New Journal of Physics*, 10, 083004
- Ofman, L., & Davila, J. M. 1998, *J. Geophys. Res.*, 103, 23677
- Okamoto, T. J., Antolin, P., De Pontieu, B., Uitenbroek, H., Van Doorselaere, T., & Yokoyama, T. 2015, *ApJ*, 809, 71
- Okamoto, T. J., & De Pontieu, B. 2011, *ApJL*, 736, L24
- Osterbrock, D. E. 1961, *ApJ*, 134, 347
- Oughton, S., Dmitruk, P., & Matthaeus, W. H. 2006, *Physics of Plasmas*, 13, 042306
- Parker, E. N. 1958, *ApJ*, 128, 664
- Perez, J. C., & Chandran, B. D. G. 2013, *ApJ*, 776, 124
- Raymond, J. C., McCauley, P. I., Cranmer, S. R., & Downs, C. 2014, *ApJ*, 788, 152
- Réville, V., & Brun, A. S. 2017, *ApJ*, 850, 45
- Roberg-Clark, G. T., Drake, J. F., Reynolds, C. S., & Swisdak, M. 2017, *ArXiv e-prints*
- Rosenthal, C. S., et al. 2002, *ApJ*, 564, 508
- Sagdeev, R. Z., & Galeev, A. A. 1969, *Nonlinear Plasma Theory*
- Shi, M., Li, H., Xiao, C., & Wang, X. 2017, *ApJ*, 842, 63
- Shiota, D., Zank, G. P., Adhikari, L., Hunana, P., Telloni, D., & Bruno, R. 2017, *ApJ*, 837, 75
- Shoda, M., & Yokoyama, T. 2016, *ApJ*, 820, 123
- . 2018, *ApJ*, 854, 9
- Shoda, M., Yokoyama, T., & Suzuki, T. K. 2018, *ApJ*, 853, 190
- Shu, C.-W., & Osher, S. 1988, *Journal of Computational Physics*, 77, 439
- Spangler, S. R. 2002, *ApJ*, 576, 997
- Spitzer, L., & Härm, R. 1953, *Physical Review*, 89, 977
- Srivastava, A. K., et al. 2017, *Scientific Reports*, 7, 43147
- Suzuki, T. K. 2004, *MNRAS*, 349, 1227
- . 2006, *ApJL*, 640, L75
- Suzuki, T. K., & Inutsuka, S.-i. 2005, *ApJL*, 632, L49
- Suzuki, T. K., & Inutsuka, S.-I. 2006, *Journal of Geophysical Research (Space Physics)*, 111, 6101
- Tenerani, A., & Velli, M. 2013, *Journal of Geophysical Research (Space Physics)*, 118, 7507
- . 2017, *ApJ*, 843, 26
- Tenerani, A., Velli, M., & Hellinger, P. 2017, *ApJ*, 851, 99
- Terasawa, T., Hoshino, M., Sakai, J.-I., & Hada, T. 1986, *J. Geophys. Res.*, 91, 4171
- Thompson, K. W. 1987, *Journal of Computational Physics*, 68, 1
- Tian, H., McIntosh, S. W., Habbal, S. R., & He, J. 2011, *ApJ*, 736, 130

- Tomczyk, S., McIntosh, S. W., Keil, S. L., Judge, P. G., Schad, T., Seeley, D. H., & Edmondson, J. 2007, *Science*, 317, 1192
- Tong, Y., Bale, S. D., Salem, C., & Pulupa, M. 2018, ArXiv e-prints
- Tu, C.-Y., & Marsch, E. 1995, *SSRv*, 73, 1
- Uchida, Y., & Kaburaki, O. 1974, *SoPh*, 35, 451
- Umeki, H., & Terasawa, T. 1992, *J. Geophys. Res.*, 97, 3113
- Usmanov, A. V., Matthaeus, W. H., Breech, B. A., & Goldstein, M. L. 2011, *ApJ*, 727, 84
- van Ballegoijen, A. A., & Asgari-Targhi, M. 2016, *ApJ*, 821, 106
- . 2017, *ApJ*, 835, 10
- van Ballegoijen, A. A., Asgari-Targhi, M., Cranmer, S. R., & DeLuca, E. E. 2011, *ApJ*, 736, 3
- van der Holst, B., Sokolov, I. V., Meng, X., Jin, M., Manchester, IV, W. B., Tóth, G., & Gombosi, T. I. 2014, *ApJ*, 782, 81
- van Leer, B. 1979, *Journal of Computational Physics*, 32, 101
- Velli, M. 1993, *A&A*, 270, 304
- Velli, M., Grappin, R., & Mangeney, A. 1991, *Geophysical and Astrophysical Fluid Dynamics*, 62, 101
- Velli, M., Grappin, R., & Mangeney, A. 1992, in *American Institute of Physics Conference Series*, Vol. 267, *Electromechanical Coupling of the Solar Atmosphere*, ed. D. S. Spicer & P. MacNeice, 154–159
- Verdini, A., Grappin, R., & Velli, M. 2012, *A&A*, 538, A70
- Verdini, A., & Velli, M. 2007, *ApJ*, 662, 669
- Verdini, A., Velli, M., & Buchlin, E. 2009, *ApJL*, 700, L39
- Verdini, A., Velli, M., Matthaeus, W. H., Oughton, S., & Dmitruk, P. 2010, *ApJL*, 708, L116
- Wang, Y.-M., & Sheeley, Jr., N. R. 1990, *ApJ*, 355, 726
- Wentzel, D. G. 1974, *SoPh*, 39, 129
- Wilhelm, K., Marsch, E., Dwivedi, B. N., Hassler, D. M., Lemaire, P., Gabriel, A. H., & Huber, M. C. E. 1998, *ApJ*, 500, 1023
- Withbroe, G. L. 1988, *ApJ*, 325, 442
- Withbroe, G. L., & Noyes, R. W. 1977, *ARA&A*, 15, 363
- Zangrilli, L., Poletto, G., Nicolosi, P., Noci, G., & Romoli, M. 2002, *ApJ*, 574, 477
- Zank, G. P., Adhikari, L., Hunana, P., Shiota, D., Bruno, R., & Telloni, D. 2017, *ApJ*, 835, 147
- Zhou, Y., & Matthaeus, W. H. 1990, *J. Geophys. Res.*, 95, 10291